SPECIAL
TRMM Diabatic Heating
COLLECTION

Spectral Retrieval of Latent Heating Profiles from TRMM PR Data. Part IV: Comparisons of Lookup Tables from Two- and Three-Dimensional Cloud-Resolving Model Simulations

SHOICHI SHIGE,* YUKARI N. TAKAYABU,+,# SATOSHI KIDA,* WEI-KUO TAO,@ XIPING ZENG,@,& CHIE YOKOYAMA,+ AND TRISTAN L'ECUYER**

* *Department of Aerospace Engineering, Osaka Prefecture University, Sakai, Osaka, Japan*
\+ *Center for Climate System Research, University of Tokyo, Kashiwa, Chiba, Japan*
\# *Institute of Observational Research for Global Change, Japan Agency for Marine-Earth Science and Technology, Yokosuka, Kanagawa, Japan*
@ *Laboratory for Atmospheres, NASA Goddard Space Flight Center, Greenbelt, Maryland*
& *Goddard Earth Sciences and Technology Center, University of Maryland, Baltimore County, Baltimore, Maryland*
** *Department of Atmospheric Science, Colorado State University, Fort Collins, Colorado*

(Manuscript received 6 November 2008, in final form 19 May 2009)

ABSTRACT

The spectral latent heating (SLH) algorithm was developed to estimate latent heating profiles for the Tropical Rainfall Measuring Mission Precipitation Radar (TRMM PR). The method uses TRMM PR information (precipitation-top height, precipitation rates at the surface and melting level, and rain type) to select heating profiles from lookup tables (LUTs). LUTs for the three rain types—convective, shallow stratiform, and anvil rain (deep stratiform with a melting level)—were derived from numerical simulations of tropical cloud systems from the Tropical Ocean and Global Atmosphere Coupled Ocean–Atmosphere Response Experiment (TOGA COARE) using a cloud-resolving model (CRM).

The two-dimensional (2D) CRM was used in previous studies. The availability of exponentially increasing computer capabilities has resulted in three-dimensional (3D) CRM simulations for multiday periods becoming increasingly prevalent. In this study, LUTs from the 2D and 3D simulations are compared. Using the LUTs from 3D simulations results in less agreement between the SLH-retrieved heating and sounding-based heating for the South China Sea Monsoon Experiment (SCSMEX). The level of SLH-estimated maximum heating is lower than that of the sounding-derived maximum heating. This is explained by the fact that using the 3D LUTs results in stronger convective heating and weaker stratiform heating above the melting level than is the case if using the 2D LUTs. More condensate is generated in and carried from the convective region in the 3D model than in the 2D model, and less condensate is produced by the stratiform region's own upward motion.

1. Introduction

A new age of active remote sensing of precipitation from space began with the launch of the Tropical Rainfall Measuring Mission (TRMM; Simpson et al. 1988, 1996; Kummerow et al. 2000), which carries the first spaceborne radar [precipitation radar (PR); Kozu et al. 2001; Okamoto 2003; Okamoto and Shige 2008]. The PR has enabled us to directly obtain vertical profiles of precipitation over the global tropics (Iguchi 2007; Iguchi et al. 2000, 2009). The high vertical resolution (250 m at nadir) and quasi-vertical beam of the PR allow it to identify a bright band for a higher percentage of all echoes than can a quasi-horizontally scanning ground radar (Schumacher and Houze 2000). Therefore, the classification between convective and stratiform regions of mesoscale convective systems (MCS) has become more straightforward, utilizing the presence of the bright band (Awaka et al. 1998, 2007, 2009).

Because differences in diabatic heating profiles exist between convective and stratiform regions of MCSs

Corresponding author address: Dr. Shoichi Shige, Division of Earth and Planetary Sciences, Graduate School of Science, Kyoto University, Kitashirakawa-Oiwake, Sakyo, Kyoto 606-8502, Japan. E-mail: shige@kugi.kyoto-u.ac.jp

DOI: 10.1175/2009JCLI2919.1

© 2009 American Meteorological Society

(Houze 1982, 1989, 1997, 2004; Johnson 1984, 2006), the accuracy of this classification is very important in estimating latent heat released by precipitating cloud systems, which is one of the key objectives of the TRMM (see a review by Tao et al. 2006). For convective regions of MCSs, the heating profile has warming at all levels with a maximum at midlevels, whereas in stratiform regions there is a warming peak in the upper troposphere and a cooling peak at low levels. The resulting MCS heating profile is positive at all levels but with a maximum value in the upper troposphere (''top heavy'' profile). Hartmann et al. (1984) demonstrated with a simple linear global model that the top-heavy heat source produces a Walker circulation that is in much better agreement with observations than those that are produced with a more conventional heat source having a maximum value in the middle troposphere. Recently, Schumacher et al. (2004) showed that the horizontal variation of the vertical distribution of heating, calculated from TRMM PR observations using a simple method, is also very important in simulating the large-scale tropical circulation correctly.

During the past four decades, cloud-resolving models (CRMs) have advanced sufficiently to allow the study of dynamic and microphysical processes associated with MCSs (see a review by Tao 2007). Chief among many significant improvements has been the addition of ice microphysical processes (e.g., Lin et al. 1983; Rutledge and Hobbs 1984). CRMs explicitly simulate the conversion of cloud condensate into raindrops and various forms of precipitation ice. These processes are not directly detectable with remote sensing (or for that matter, with in situ measurements). Thus heating retrieval schemes depend heavily on the use of a CRM. The advent of powerful computers allows us to run CRMs with resolutions fine enough to represent individual cloud elements and space–time domains large enough to encompass many clouds over many cloud lifetimes; this is so-called cloud ensemble modeling (e.g., Yamasaki 1975; Soong and Ogura 1980; Soong and Tao 1980; Tao and Soong 1986; Nakajima and Matsuno 1988; Xu 1993; Grabowski et al. 1996). The CRM is now at a stage where it can provide reasonably accurate statistical information of cloud-scale processes and thus is one of the most important tools used to establish the quantitative relationship between the latent heating profile and precipitation profile.

The spectral latent heating (SLH) algorithm has been developed for the TRMM PR using a CRM (Shige et al. 2004, 2007; hereafter, Part I and Part II). The previous methods considers only rain types (convective or stratiform), based on the assumption that the shape of the overall MCS heating profile is determined by the relative amounts of convective and stratiform heating (Tao et al. 1993a; Schumacher et al. 2004). In these bulk methods, the variation of rain depth is not taken into account. On the other hand, the SLH algorithm considers not only rain types but also a spectrum of precipitation profiles as a function of precipitation-top height (PTH), based on a spectral expression of TRMM PR precipitation profiles by Takayabu (2002). Heating profile lookup tables (LUTs) for the three rain types—convective, shallow stratiform, and anvil rain (deep stratiform with a melting level)—were produced from numerical simulations of tropical cloud systems in the Tropical Ocean and Global Atmosphere Coupled Ocean–Atmosphere Response Experiment (TOGA COARE; Webster and Lukas 1992). For convective and shallow stratiform regions, the LUT is based on the PTH. Considering the sensitivity of the PR, we used a threshold of 0.3 mm h^{-1} to determine the PTH. Properties (i.e., shape and magnitude) of the convective and shallow stratiform heating profiles show near-monotonic change with the PTH, suggesting that the distribution of latent heating is a strong function of the PTH. On the other hand, the PR cannot observe the PTH with sufficient accuracy for anvil regions because of its insensitivity to the small ice-phase hydrometeors (Heymsfield et al. 2000). The anvil heating profile shape is much more uniform in time and space than the convective heating profile in the MCSs (Houze 1989), such that the height of maximum anvil heating is not overly sensitive to the storm-height observation. Thus for an anvil region, the LUT is based on the precipitation rate at the melting level P_m instead of the PTH. The SLH estimates from PR data were in good agreement with rawinsonde estimates averaged over the Northern Enhanced Sounding Array (NESA) of the 1998 South China Sea Monsoon Experiment (SCSMEX; Lau et al. 2000). Recently, the work by Shige et al. (2008; hereafter, Part III) used the SLH algorithm to estimate the vertical distribution of the apparent moisture sink. Although discrepancies between the SLH-retrieved and sounding-based profiles of the apparent moisture sink for the SCSMEX NESA were larger than those for heating, key features of the vertical profiles agreed well.

The two-dimensional (2D) CRM was used in Parts I, II, and III. Observed large-scale advective tendencies of temperature, moisture, and horizontal momentum were used as the main large-scale forcings that govern the CRM in a semiprognostic manner (Soong and Ogura 1980). The availability of exponentially increasing computer capabilities has resulted in three-dimensional (3D) CRM simulations for multiday periods with large horizontal domains becoming increasing prevalent. Although real clouds and cloud systems are 3D, a 3D CRM does not automatically give more realistic simulation than a

2D CRM does. This is because the results of the simulation depend very strongly on incomplete and uncertain parameterizations of ice microphysical processes. Considerable effort has been devoted in recent years to evaluating the performance of CRMs using the TRMM observation. Most previous studies focused on 3D CRMs (e.g., Bauer 2001; Wiedner et al. 2004; Biggerstaff et al. 2006; Seo and Biggerstaff 2006; Zhou et al. 2007). Comparisons between 2D and 3D CRMs based on TRMM observations have not been done. Whether a 2D CRM is acceptable is an old issue (e.g., Wilhelmson 1974; Schlesinger 1984), but still an important one for climate simulations where a CRM is run as a "superparameterization" [or multiscale modeling framework (MMF)] (Grabowski and Smolarkiewicz 1999; Grabowski 2001) inside a global circulation model (GCM), as discussed by Randall et al. (2003). In this study, the PR heating estimates from the SLH algorithm using LUTs produced from the 2D and 3D CRM simulations are compared with heating profiles derived diagnostically from sounding data. Such a comparison might be useful not only for the SLH algorithm but also for climate simulations with superparameterization (or MMF) as well as a new cumulus parameterization, for which the use of lookup tables replaces traditional parameterizations (Pielke et al. 2006, 2007).

2. Approach

In diagnostic studies (Yanai et al. 1973; Yanai and Johnson 1993), it is customary to define the apparent heat source Q_1 of a large-scale system by averaging horizontally the thermodynamic and water vapor equations:

$$Q_1 = \overline{\pi}\left(\frac{\partial\overline{\theta}}{\partial t} + \overline{\mathbf{v}}\cdot\nabla\overline{\theta} + \overline{w}\frac{\partial\overline{\theta}}{\partial z}\right), \qquad (1)$$

where θ is the potential temperature, $\mathbf{v}$ the horizontal velocity, w the vertical velocity, $\pi = (p/P_{00})^{R/C_p}$ the nondimensional pressure, p the pressure, P_{00} the reference pressure (1000 mb), C_p the specific heat of dry air at constant pressure, and R the gas constant for dry air. The overbars denote horizontal averages.

The Q_1 can be directly related to the contributions of cloud effects, which can be explicitly estimated by CRMs, by

$$Q_1 = \overline{\pi}\left(-\frac{1}{\overline{\rho}}\frac{\partial\overline{\rho}\overline{w'\theta'}}{\partial z} - \overline{\mathbf{v}'\cdot\nabla\theta'} + \overline{D}_\theta\right) + \overline{\mathrm{LH}} + \overline{Q}_R. \qquad (2)$$

The primes indicate deviations from the horizontal averages; $\bar{\rho}$ is the air density and Q_R the cooling/heating rate associated with radiative processes. The subgrid-scale (smaller than the cloud scale) diffusion is represented by D_θ, which is usually small compared with other terms above the boundary layer (Soong and Tao 1980). The term LH is the net latent heating due to the phase change of water:

$$\mathrm{LH} = \frac{L_v}{C_p}(c-e) + \frac{L_f}{C_p}(f-m) + \frac{L_s}{C_p}(d-s), \qquad (3)$$

where L_v, L_f, and L_s are the latent heats of vaporization, fusion, and sublimation, respectively. Variables c, e, f, m, d, and s are the rates of condensation of cloud droplets; evaporation of cloud droplets and raindrops; freezing of cloud droplets and raindrops; melting of ice crystals, snow, and graupel; deposition of ice crystals; and sublimation of all ice hydrometeors, respectively. The first term on the right-hand side of Eq. (2) is the vertical eddy heat flux convergence from upward and downward cloud-scale motions, while the second term is the horizontal eddy heat flux convergence. The precipitation falling at a given time is not related to the heating/cooling that is occurring at that instant but rather to the accumulated heating/cooling that led up to the precipitation over a finite time period. Thus we accumulate $Q_1 - Q_R$ (hereinafter Q_{1R}) over a period of 5 min for each data sampling, since accumulation over long periods is inadequate for growing convective cells (Shige and Satomura 2000, their Fig. 4a) and fast-moving convective systems. The SLH algorithm estimates Q_{1R} mainly caused by precipitation processes (Q_{1Rp}), because it is severely limited by the inherent sensitivity of the PR that can detect only precipitation-sized particles.

The CRM used in this study is the Goddard Cumulus Ensemble (GCE) model (Tao and Simpson 1993) as used in Parts I, II, and III, but both 2D and 3D versions are used here. Recent improvements were presented by Tao et al. (2003a). Numerical simulations were conducted with the version 2.1 TOGA COARE forcing dataset (Ciesielski et al. 2003), which uses the latest humidity corrected sonde data (Wang et al. 2002) in which a low-level dry bias in the original Vaisala sonde data was reduced. Ciesielski et al. (2003) have shown that the difference between observed enthalpy changes the 120-day time integral of TOGA COARE data-derived enthalpy forcing, which was pointed out by Emanuel and Zivkovic-Rothman (1999) and Wu et al. (2000), was reduced substantially (from 25 to 5 K). For the 2D simulations, a 1024-km horizontal domain was covered by 1024 grids with a horizontal grid spacing of 1 km. For the 3D simulations, the 256 × 256-km horizontal domain was covered by 128 × 128 grids with a horizontal grid spacing of 2 km. Test 3D simulations with a 1-km horizontal grid spacing indicated that basic features did not

change with the change in resolution. For both 2D and 3D simulations, a stretched vertical coordinate (height increments from 80 m near the surface to 1000 m at the top of the domain) with 41 levels was used to maximize resolution at low levels. The depth of the domain was 22.4 km. Note that the 2D simulations in this study are not the same as in Part II. The 2D simulations in this study were made with the TOGA COARE flux algorithm (Fairall et al. 1996; Wang et al. 1996) and a modification of conversion of cloud ice to snow in the ice microphysics schemes (Tao et al. 2003a) as well as the 3D simulations. The 2D and 3D simulations have been done with data sampling frequency of 5 and 15 min, respectively.

The accuracy of the convective–stratiform separation affects the determination of the vertical distribution of heating. The TRMM PR rain-type classifications, in which brightband identification is very important, cannot be directly applied to GCE outputs (Awaka et al. 1996). The microphysical schemes used in CRMs (e.g., Lin et al. 1983; Rutledge and Hobbs 1984) typically do not contain an explicit description of the partially melted precipitation particles that lead to a bright band of enhanced radar reflectivity. Thus the GCE convective and stratiform separation method (Lang et al. 2003) is used with modifications described in Part I to maintain the consistency with the TRMM PR version 6 2A23 convective–stratiform separation algorithm (Awaka et al. 2007, 2009). Considering the sensitivity of the PR, we classified model grid points that have a precipitation less than a threshold of 0.3 mm h^{-1} as a nonprecipitating region.

In this paper, LUTs are derived from 2D and 3D CRM simulations from TOGA COARE, and then they are used to obtain the SLH heating estimates from PR data. The results are compared with heating profiles derived diagnostically from sounding data from another field campaign. Heating profiles have been calculated from sounding networks and other observations during three TRMM field campaigns [the Kwajelein Experiment (KWAJEX), TRMM Large-Scale Biosphere–Atmosphere Experiment in Amazonia (LBA), and SCSMEX] by Schumacher et al. (2007), using the variational analysis approach of Zhang and Lin (1997). The variational analysis constrains the sounding data to satisfy column-integrated budgets of mass, energy, and moisture. Since ground radar precipitation maps are generally used as one of the analysis constraints, the size of the variational analysis domain is much smaller than the domain size of the sounding networks for carrying out the traditional budget studies. The sampling errors in PR estimates from the SLH algorithm naturally decreases as the results are averaged over larger areas, thus sounding-only retrieval is used for comparison in this study.

TABLE 1. Domain-averaged surface rainfall amounts (mm day^{-1}) estimated from data of the sounding network and the TRMM PR for the SCSMEX NESA and SCSMEX SESA.

	SCSMEX NESA	SCSMEX SESA
	15 May–20 Jun 1998	5 May–20 Jun 1998
Sounding	10.2	5.4
TRMM PR	9.4	3.4

The sampling errors in sounding-array budgets also decrease as the results are averaged over longer time periods. The analysis domains for the SCSMEX are much larger than those for the KWAJEX and TRMM LBA. There were two enhanced sounding arrays during the SCSMEX: the NESA (Johnson and Ciesielski 2002) and Southern Enhanced Sounding Array (SESA) (Ciesielski and Johnson 2006). Mapes et al. (2003) suggested that averages of about 30 days reduce sampling errors in the rainfall rate estimate (proportional to integrated Q_1) from a moisture budget to 10% for the SCSMEX NESA. The surface rainfall from soundings and the TRMM PR over the SCSMEX NESA for the 37-day period from 15 May to 20 June and over the SCSMEX SESA for 47-day period from 5 May to 20 June are shown in Table 1. These periods were chosen following Johnson and Ciesielski (2002) and Ciesielski and Johnson (2006). The differences in the surface rainfall (proportional to integrated Q_1) between sounding and PR estimates are 8% over the SCSMEX NESA region and 45% over the SCSMEX SESA region. Although the analysis domain for the SCSMEX SESA is nearly the same as that for the SCSMEX NESA, the number of overpasses for the SCSMEX SESA is less than that for the SCSMEX NESA because of less sampling at lower latitudes in the TRMM (see Fig. 1 of Negri et al. 2002). The larger sampling errors for PR estimates lead to a larger discrepancy in the sounding estimates for the SCSMEX SESA than in the estimates for the SCSMEX NESA. Therefore, only the heating profiles from sounding data of the SCSMEX NESA are used as validation in this study.

The total errors in the satellite estimates consist of sampling errors and algorithm errors. The algorithm errors contain random and systematic components. Yang et al. (2006) suggested that sampling error represents only a portion of the total error in monthly 2.5°-resolution TRMM Microwave Imager (TMI) rain estimates. They also suggested that the contribution from systematic algorithm errors is often greater in magnitude than that of random algorithm errors at this time–space resolution. Although the PR estimates are more subject to sampling errors due to the PR's narrow swath width (~215 km) than TMI estimates, the algorithm errors,

in particular the algorithm systematic errors, could make a important contribution to the estimates averaged over the SCSMEX NESA (~10.0° × 6.0°) and the 37-day period. Systematic algorithm errors arise from the physical inconsistency or nonrepresentativeness of CRM-simulated profiles that support the lookup tables of the SLH algorithm. In Part II, the universality of the lookup tables from the TOGA COARE simulations (i.e., representativeness of CRM-simulated profiles) was examined for its application to PR data over tropical ocean regions. Lookup tables were produced from 2D simulations from the Global Atmospheric Research Program (GARP) Atlantic Tropical Experiment (GATE), SCSMEX, and KWAJEX, and the similarity in the lookup tables from case to case was evident. Improvements were made to the SLH algorithm, taking into account two factors: differences in the vertical distribution of deep convective heating due to the relative importance of liquid and ice water processes that varies from case to case, and differences in the level separating upper-level heating and lower-level cooling. In the present study, we focus on the physical consistency of the 2D and 3D CRM simulations from TOGA COARE that support the lookup tables.

For a more rigorous test, the SLH algorithm should be applied to ground radar data and the results compared with heating profiles derived using the variational method whose domains generally coincide with ground radar coverage. Such a test is optimal from a sampling perspective. In particular, comparisons using the data from the KWAJEX and TRMM LBA are very important, because the SCSMEX NESA region, which was chosen here, was heavily influenced by MCSs as was the TOGA COARE region, and it is not necessarily representative of Kwajelein and the Amazon. However, such comparisons are beyond the scope, and are left to future studies.

3. Results

a. General features

Domain-averaged surface rainfall amounts and stratiform percentages from the GCE 2D and 3D models for the TOGA COARE episode are shown in Table 2. The model results indicate that the stratiform rain percentage is not greatly affected by the dimensionality of the model. The reason for the similarity between the GCE 2D and 3D simulations is that the same observed, large-scale advective tendencies of potential temperature, water vapor mixing ratio, and horizontal momentum were used as the main forcing in both models.

Figures 1a–c show the time series of Q_1 profiles averaged over the TOGA COARE Intensive Flux Array (IFA) region for the 19–26 December 1992 period derived diagnostically from soundings (Ciesielski et al. 2003), GCE 2D simulations, and GCE 3D simulations. A 15-min running mean is applied to the 2D data with sampling frequency of 5 min for the comparison. The pattern of temporal variability among Q_1 profiles from soundings, GCE 2D simulations, and GCE 3D simulations is quite good. However, there exists larger temporal variability of Q_1 profiles in the 2D simulation than in the 3D simulation, which is consistent with the results found by Grabowski et al. (1998), Donner et al. (1999), and Zeng et al. (2007), because the rapid fluctuation in surface precipitation is associated with the rapid fluctuation in the vertically integrated Q_1.

TABLE 2. Domain-averaged surface rainfall amounts and stratiform percentages from the GCE 2D and 3D models for the TOGA COARE episode. Rainfall estimated by the sounding network is also shown.

	Rainfall (mm day^{-1})	Stratiform (%)
GCE 2D	19.86	43
GCE 3D	18.98	40
Sounding	19.91	—

In this study, we focus on the heating profiles, but the apparent moisture sink Q_2 profiles, corresponding to the Q_1 profiles (Figs. 1a–c), are also shown in Figs. 1d–f. Although the same observed, large-scale advective tendencies of potential temperature, water vapor mixing ratio, and horizontal momentum were used as the main forcing in both models, the Q_2 profiles in the 3D simulation (Fig. 1f) are in better agreement with observations (Fig. 1d) in the lower troposphere than those in the 2D simulation (Fig. 1e), as pointed out by Tao et al. (2000). The Q_2 profiles in the 2D simulation show fluctuation with larger amplitudes in the lower troposphere than those in the 3D simulation and observations. While the contribution to the Q_1 budget by the eddy heat flux convergence is minor, the eddy moisture flux convergence is one of the major contributors to Q_2 (Part III), leading to differences in the Q_2 profiles between the 2D and 3D simulations. Better agreement of the Q_2 profiles in the 3D simulation with observations is due to the fact that the turbulent processes in the planetary boundary layer is three-dimensional in nature, and it is very important for Q_2 retrieval using the SLH algorithm (Part III), which motivates us to produce LUTs using GCE 3D simulations.

b. Comparisons of lookup tables

Figure 2a shows an LUT produced from GCE 2D simulations (hereinafter LUT2D) for convective rain. In Part I, Part II, and Part III, the GCE-simulated precipitation profiles and corresponding heating profiles from

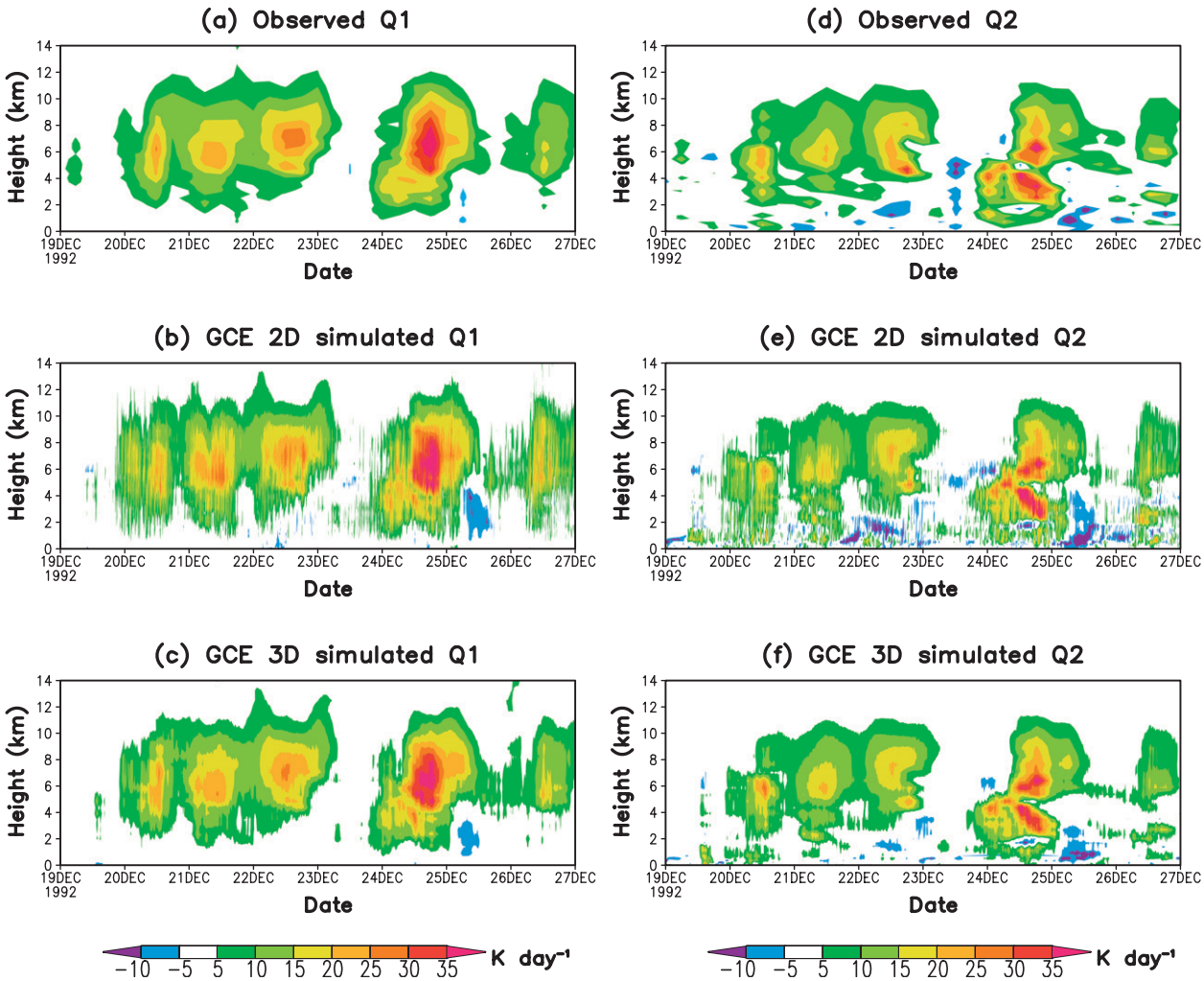

FIG. 1. Time series of Q_1 and Q_2 profiles averaged over the TOGA COARE IFA region for the 19–26 Dec 1992 period: (a) Q_1 and (d) Q_2 derived diagnostically from soundings (Ciesielski et al. 2003); (b) Q_1 and (e) Q_2 simulated by the GCE 2D model; (c) Q_1 and (f) Q_2 simulated by the GCE 3D model.

the four subperiods of 9 days each (10–18 December 1992, 27 December 1992–4 January 1993, 9–17 February 1993, and 18–26 February 1993) were used for construction of lookup tables, and another simulation for the one subperiod of 8 days each (19–26 December 1992; Fig. 1b) was used for the consistency check of the algorithm. In this study, the simulation for the subperiod of 8 days is also used for construction of lookup tables. The GCE-simulated precipitation profiles with a 0.3 mm h^{-1} precipitation-top threshold and corresponding heating profiles are accumulated and averaged for each PTH with model grid intervals. Properties (i.e., shape and magnitude) of the convective heating profiles show near-monotonic changes with PTH. The heating-top height is determined by the PTH. The shallow convective heating profiles (PTH $<$ 6 km) are characterized by cooling aloft due to an excess of evaporation over condensation, such as in trade wind cumulus (Nitta and Esbensen 1974). Recently, Schumacher et al. (2008) isolated Q_1 in different cloud types during KWAJEX and showed cooling above both the shallow cumulus and cumulus congestus. The shallow convective heating profile shape in the LUT2D is consistent with the observational result of Schumacher et al. (2008). Another interesting feature is that the convective heating profiles for the highest PTH are also characterized by cooling aloft. This feature is consistent with the strong cooling above mesoscale convective systems observed by Johnson and Kriete (1982) and Lin and Johnson (1996). More recent discussion of the cooling above deep convection is in Holloway and Neelin (2007).

Figure 2b shows an LUT2D for anvil (deep stratiform with a PTH higher than the melting level) rain. The PR can measure the precipitation rate at the melting level,

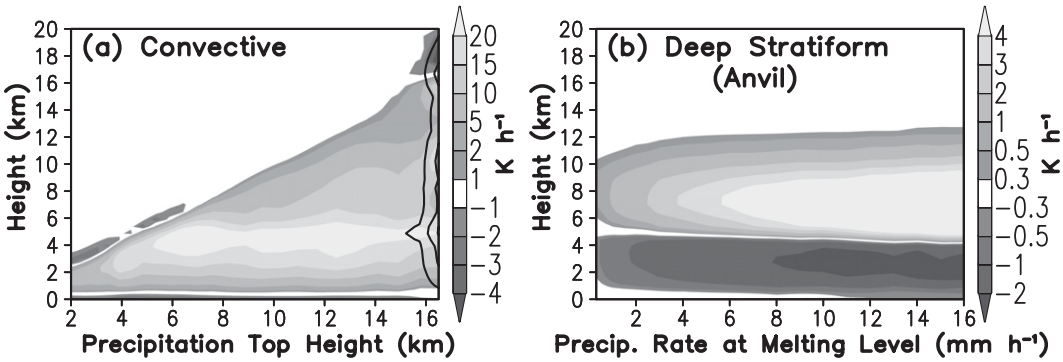

FIG. 2. Lookup tables of Q_{1Rp} profiles for the (a) convective and (b) deep stratiform (anvil) regions derived from the TOGA COARE simulations using the GCE 2D model (LUT2D). Contours indicate confidence intervals for a mean at the 95% level using the Student's t test. The contour interval is 2.0 K h^{-1}.

as can surface-based radar (e.g., Leary and Houze 1979), although it cannot observe the PTH with sufficient accuracy in the upper-level regions of the anvils because of its insensitivity to the small ice-phase hydrometeors (Heymsfield et al. 2000). Thus, for the anvil region, the LUT refers to the precipitation rate at the melting level P_m instead of the PTH (Part I). The deep stratiform profiles with a PTH higher than the melting level are characterized by upper-level heating and lower-level cooling, which was also found in observations (e.g., Johnson and Young 1983). The upper-level heating in these anvil regions is largely due to condensation and deposition, while the lower-level cooling is largely due to evaporation of raindrops and melting of ice particles (Leary and Houze 1979). A set maximum height for Q_{1R} profiles can be seen around 12 km.

Figure 3a shows an LUT produced from GCE 3D simulations (hereinafter LUT3D) for convective rain. The GCE-simulated precipitation profiles and corresponding heating profiles from the same subperiods as for the LUT2D were used for construction of lookup tables. As for the LUT2D, the heating-top height is determined by the PTH. The shallow convective heating profiles (PTH $<$ 6 km) are characterized by cooling aloft due to an excess of evaporation over condensation, and the convective heating profiles for the highest PTH are also characterized by cooling aloft. Although a 2-km horizontal grid spacing and relatively poor vertical resolution are used, the shallow convective heating profile shape in LUT3D is also consistent with the observational results (Nitta and Esbensen 1974; Schumacher et al. 2008). On the other hand, differences in vertical structure (e.g., the level of maximum Q_{1Rp} heating) for a given PTH between the LUT2D and LUT3D are distinct. Figure 4a shows that the 3D convection with PTH higher than 10 km has much stronger heating above the melting level (4.4 km) than the 2D convection does, while the 3D convection with PTHs between 4 and 8 km (cumulus congestus) has weaker heating just below the heating-top height (Fig. 4a). In the LUT2D, the level of the Q_{1R} heating peak shifts upward until the PTH reaches 6 km, and then plateaus around the melting level (Fig. 2a). On the other hand, in the LUT3D, the level of the Q_{1R} heating peak for a PTH higher than 6 km is well above the melting level (Fig. 3a). These results indicate that liquid water processes dominate in the GCE 2D simulations, while ice water processes dominate in the GCE 3D simulations.

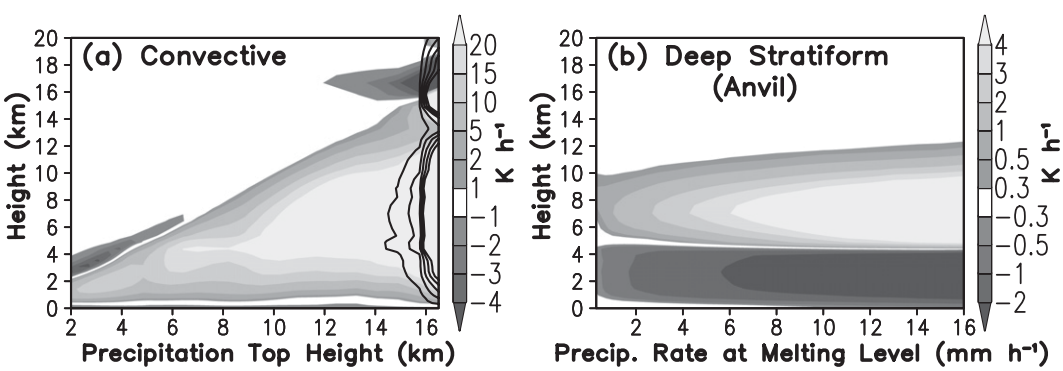

FIG. 3. As in Fig. 2, but using the GCE 3D model (LUT3D).

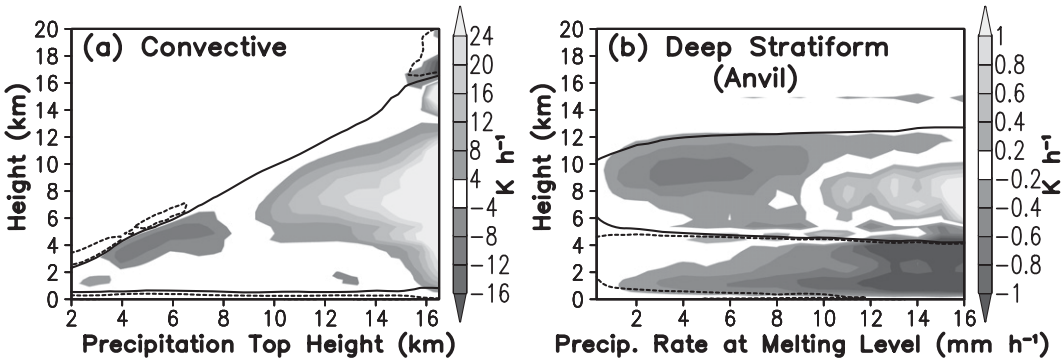

FIG. 4. The Q_{1Rp} profiles in LUT3D shown in Fig. 3 minus those in LUT2D shown in Fig. 2. For reference, solid contours indicate regions with heating (≥ 1 K h^{-1}) for LUT2D, while dashed contours indicate regions with cooling (≤ -1 K h^{-1}) for LUT2D.

Figure 3b shows an LUT produced from GCE 3D simulations for anvil (deep stratiform with a PTH higher than the melting level) rain. As for the LUT2D, the deep stratiform profiles with a PTH higher than the melting level are characterized by upper-level heating and lower-level cooling. Figure 4b shows that the 3D anvil rain has weaker upper-level heating than the 2D anvil rain, indicating that the set maximum height for Q_{1R} profiles in the LUT3D for the deep stratiform is lower than that in the LUT2D. The 3D anvil rain with P_m smaller than 10 mm h^{-1} has weaker heating at all levels above the melting level than 2D anvil rain does, while the 3D anvil rain with P_m larger than 10 mm h^{-1} has stronger heating at z = 6–9 km. On the other hand, the 3D anvil rain has stronger lower-level cooling than the 2D anvil rain.

Note that LUTs for shallow stratiform rain were produced from GCE 2D and 3D simulations, but the differences between LUT2D and LUT3D for shallow stratiform rain are small. The contribution by shallow stratiform rain to heating estimates is also small. Therefore we will not discuss shallow stratiform rain, and hereinafter deep stratiform (anvil) rain is just represented as stratiform rain.

c. *Comparison of Q_1 profiles over the SCSMEX NESA region*

A sounding-based analysis of diabatic heating for the SCSMEX NESA derived by Johnson and Ciesielski (2002) was used to evaluate the accuracy of the heating estimates from the TRMM (Magagi and Barros 2004; Grecu and Olson 2006; Yang et al. 2006; Part II). Figure 5 shows a comparison between SLH-retrieved Q_{1Rp} (Q_{1R} for precipitation regions) from version 6 of the TRMM PR datasets using the LUT2D and sounding-based Q_1 during the campaign's most convectively active period (15 May–20 June 1998). This period also coincides with the time when the budget analysis was considered most reliable because of the completeness of the sounding network. The heating profile derived using the variational analysis of Zhang and Lin (1997) is similar to that derived by Johnson and Ciesielski (2002) but is more bottom heavy, probably because of different analysis domains. Note that the SLH-retrieved Q_{1Rp} profiles are not the same as in Part II, because the LUTs in this study are not the same as in Part II. Differences in heights above sea level over land (i.e., terrain) are also taken into account by the SLH algorithm used in this study. As

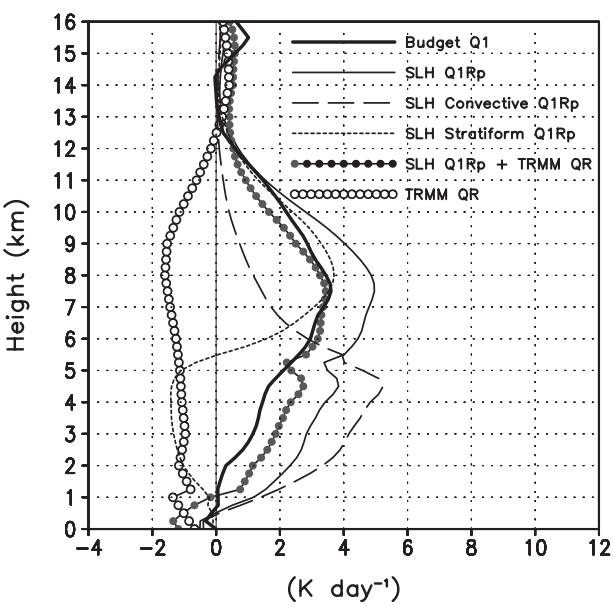

FIG. 5. Mean heating from diagnostic calculations for the SCSMEX (15 May–20 Jun 1998) (Johnson and Ciesielski 2002) and the SLH algorithm using lookup tables derived from the TOGA COARE simulations using the GCE 2D model.

pointed out in Part II, key features of the vertical profiles agree well, particularly the level of maximum heating. In the tropics, cloud radiative forcing makes the largest contribution to the total diabatic heating after latent heating. Tao et al. (2003b, 2004) reported that net radiation (cooling) accounts for about 20% or more of the net condensation for the SCSMEX cloud systems simulated by the GCE model. The vertical profile of Q_R can be estimated from the TMI and Visible and Infrared Scanner (VIRS) aboard the TRMM (L'Ecuyer and Stephens 2003). The vertical profile of Q_R estimated from the TRMM for the SCSMEX NESA (15 May–20 June 1998) is shown on the left side of the figure. These TRMM Q_R estimates are very similar to the GCE 2D Q_R simulations for the SCSMEX periods (18–26 May 1998 and 2–11 June 1998) shown in Fig. 11 of Part II and are added to the SLH-retrieved Q_{1Rp} estimates. The level of maximum heating of $Q_{1Rp} + Q_R$ and its magnitude are in very good agreement with the sounding-derived Q_1. It is evident from Fig. 5 that, in the lower troposphere, the $Q_{1Rp} + Q_R$ heating magnitudes are about 1 K greater than the sounding-derived magnitudes, because the SLH-estimated convective $Q_{1Rp} + Q_R$ heating magnitudes are larger than the SLH-estimated stratiform $Q_{1Rp} + Q_R$ cooling magnitudes. As discussed in Part II, the heating estimates are sensitive to the estimated fraction of stratiform rainfall from the PR data, and sampling errors may account for the overestimation of $Q_{1Rp} + Q_R$ heating in the lower troposphere (see Fig. 12 in Part II).

Positive (negative) isentropic potential vorticity can be generated where Q_1 increases (decreases) with height (Haynes and McIntyre 1987), thus the vertical heating gradient is the dynamically important quantity. Figure 6 shows a comparison between vertical gradients of Q_{1Rp} and $Q_{1Rp} + Q_R$ retrieved by the SLH algorithm using the LUT2D and those of sounding-based Q_1. They are in good agreement except for the lowest level (~1 km), the middle level (~5 km), and the upper level (~15 km). The discrepancy at the lowest level may be explained by the fact that the SLH algorithm cannot estimate the latent heating profile of a nonprecipitating cumulus cloud, which is positive in the lower part of the cloud because of net positive condensation and negative in the upper part of the cloud where detrainment occurs and evaporation exceeds condensation (Nitta and Esbensen 1974; Johnson and Lin 1997). The middle level having the discrepancy corresponds to the melting level where maximum convective heating and maximum stratiform cooling exist. The heating estimates at the melting level are very sensitive to the estimated fraction of stratiform rainfall from the PR data. Thus sampling errors may account for the discrepancy at the middle level. At the upper level, the radiative cooling must be balanced by deep convection. Since the saturation mixing ratio is low at the upper level, deep convection heats the upper troposphere largely by eddy heat flux convergence (Sui et al. 1994; Mapes 2001). Thus the discrepancy at the upper level may be explained by the fact that the SLH algorithm cannot estimate eddy heat flux convergence associated with deep convection because of sampling errors and the inherent sensitivity of the PR, which can detect only precipitation-sized particles.

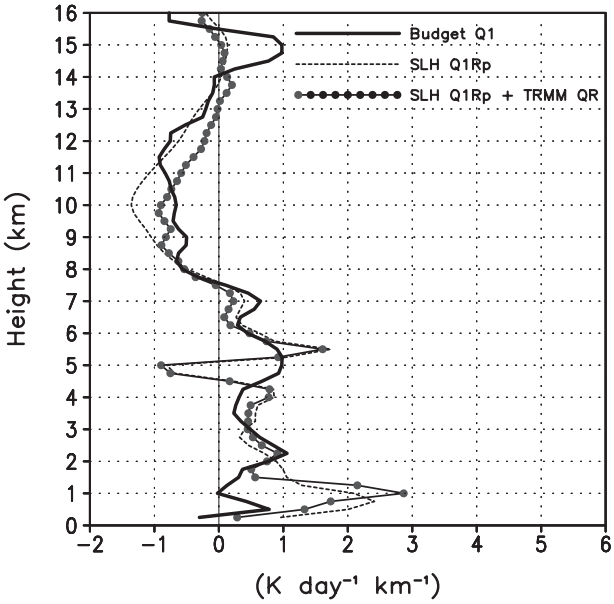

FIG. 6. Vertical heating gradients from diagnostic calculations for the SCSMEX (15 May–20 Jun 1998) (Johnson and Ciesielski 2002) and the SLH algorithm using lookup tables derived from the TOGA COARE simulations using the GCE 2D model.

Figure 7 shows a comparison between SLH-retrieved Q_{1Rp} using the LUT3D and sounding-based Q_1. Using the LUT3D leads to less agreement between the SLH-retrieved Q_{1Rp} and sounding-based Q_1. The level of maximum heating of $Q_{1Rp} + Q_R$ is slightly lower than that of the sounding-derived Q_1. The $Q_{1Rp} + Q_R$ magnitude at z = 4–8 km is larger than the sounding-derived Q_1. Vertical gradients of Q_{1Rp} and $Q_{1Rp} + Q_R$ retrieved by the SLH-retrieved Q_{1Rp} algorithms using the LUT3D (Fig. 8) are also less in agreement with those of sounding-based Q_1 compared with the case for the 2D counterparts.

4. Discussion

To investigate why discrepancies between the SLH-retrieved heating estimates and sounding-based estimates for the LUT3D are larger than those for the

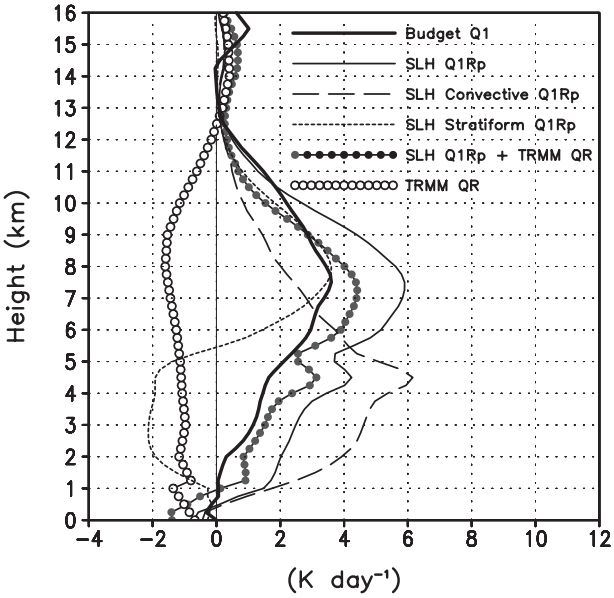

FIG. 7. As in Fig. 5, but for the SLH algorithm using lookup tables derived from the TOGA COARE simulations using the GCE 3D model.

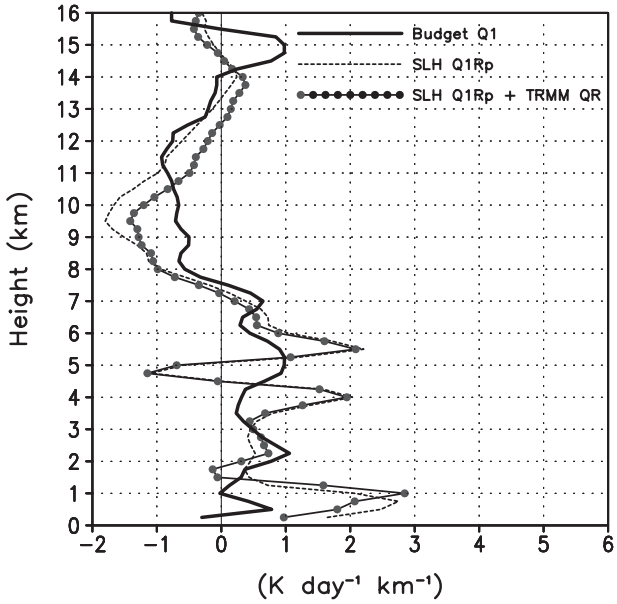

FIG. 8. As in Fig. 6, but for the SLH algorithm using lookup tables derived from the TOGA COARE simulations using the GCE 3D model.

LUT2D, we examine the differences between the heating profiles for the LUT2D and LUT3D. Figure 9 shows Q_{1Rp} and precipitation profiles with selected PTH values of 3.1, 5.9, 10.2, and 14.0 km from the convective LUT2D and LUT3D. Note that the Q_{1Rp} profiles and precipitation profiles are normalized by the near-surface rain rate. The vertical structure (e.g., maximum heating level) of the convective heating profiles with the PTH being lower than 10 km does not vary between the 2D and 3D models. However, the differences between convective heating profile shapes for the 2D and 3D models increase with the PTH being higher than 10 km. The 3D convection has stronger heating above the melting level than the 2D convection does. Similarly, the differences between corresponding precipitation profile shapes for 2D and 3D models also increase with the PTH being higher than 10 km. The 3D convection has stronger precipitation intensity above the melting level than 2D convection does. This modeling phenomenon is consistent with the previous conclusion that there are more convective cores with strong updrafts in a 3D model than in its 2D counterpart (e.g., Phillips and Donner 2006; Zeng et al. 2008), and it is attributed to the difference in the response of vertical circulation to thermal forcing between the two kinds of models. The differences in convective heating and precipitation profile shapes between the 2D and 3D simulations from the TOGA COARE are much larger than those among the TOGA COARE, GATE, SCSMEX, and KWAJEX simulations (Fig. 6 of Part II).

Previous ground-based observations of oceanic convection over both the Pacific and Atlantic basins (e.g., Szoke et al. 1986; Jorgensen and LeMone 1989; Zipser and Lutz 1994; Takahashi et al. 1995; DeMott and Rutledge 1998) and recent TRMM observations of convection over all of the oceanic basins (e.g., Nesbitt et al. 2000; Petersen and Rutledge 2001; Takayabu 2002, 2006) suggest that the primary precipitation mechanism in deep oceanic convection is the liquid water processes. Therefore, the 2D convection has better consistency with these observations than does the 3D convection. Note that the differences in heating and precipitation profile shape below the melting level between the 2D and 3D models are very small. These results suggest that ice microphysical processes are affected greatly by the dimensionality of the modeling, but liquid microphysical processes are not affected.

Figure 10 shows GCE-simulated Q_{1Rp} and precipitation profiles with selected P_m values of 2.0, 4.0, 8.0, and 16 mm h^{-1} from the stratiform LUT2D and LUT3D. The upper-level stratiform heating in the 3D model for weaker P_m (i.e., 2.0 and 4.0 mm h^{-1}) is weaker than its 2D counterpart. Although the discrepancy decreases with P_m, the number of pixels observed by the PR for weaker P_m is much larger than the number for stronger P_m. Thus the SLH algorithm with the LUT3D estimates weaker heating amplitude in stratiform heating, resulting

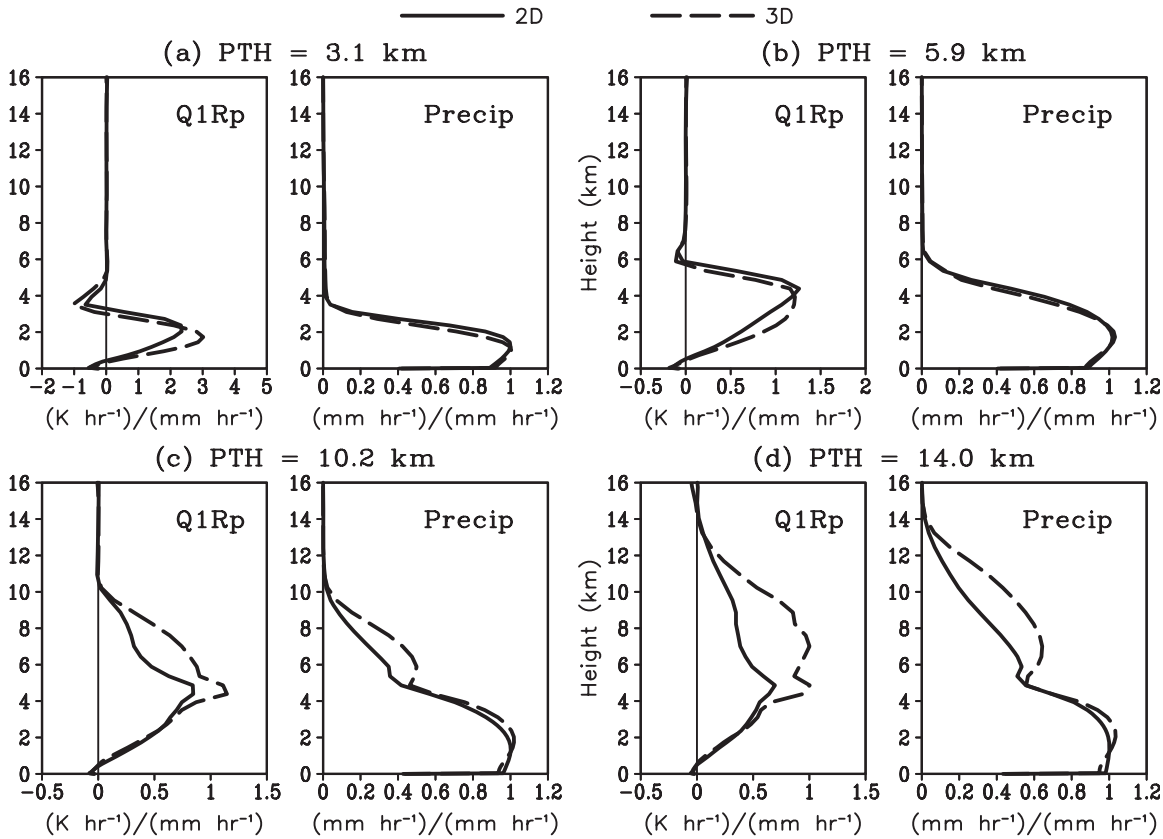

FIG. 9. Ensemble-mean GCE-simulated Q_{1Rp} and precipitation profiles with the selected PTH values of (a) 3.1 km, (b) 5.9 km, (c) 10.2 km, and (d) 14 km from the convective regions of 2D and 3D simulations. The Q_{1R} and precipitation profiles are normalized by the near-surface rain rate.

in underestimation of the level of maximum heating (Fig. 7). On the other hand, as indicated in Fig. 4b, the 3D anvil rain has stronger lower-level cooling than the 2D anvil rain, although the decrease of rain rate from the melting level to the surface is smaller in 3D than 2D. These differences between LUT2D and LUT3D cause differences in the low-level cooling profiles in Figs. 5 and 7. The deep stratiform profiles should be greatly affected by the mesoscale circulation in the stratiform region, including an ascending front-to-rear flow, a midlevel rear inflow, and a mesoscale up- and downdraft. Pandya and Durran (1996) revealed that the mesoscale circulation in the stratiform region is the result of gravity waves forced by the low-frequency components of the latent heating and cooling in the leading convective line and that the circulation shows a great sensitivity to variations in the thermal forcing in the convective line. Thus, differences in heating profiles between the stratiform LUT2D and LUT3D are probably due to differences in the mesoscale circulation in the stratiform region, which are caused by the differences in heating profiles between the convective LUT2D and LUT3D.

Houze et al. (1980), Gamache and Houze (1983), and Chong and Hauser (1989) showed that the stratiform precipitation falling into the melting layer from the anvil cloud above is a combination of condensate generated in and carried from the convective region plus condensate that is produced by the anvil region's own upward motion by analyzing the water budgets of a precipitating tropical mesoscale convective system. To evaluate this advection effect, we calculated the following values for the LUT2D and LUT3D:

$$R_{\mathrm{conv}} = \frac{C_p}{L_v}\int_0^{z_t} \frac{\rho\widetilde{Q_{1Rp}}(z)\Delta z}{\widetilde{P}_s} = 1 + f, \quad \text{and} \tag{4}$$

$$R_{\mathrm{stra}} = \frac{C_p}{L_v}\int_{z_m}^{z_t} \frac{\rho\widetilde{Q_{1Rp}}(z)\Delta z}{\widetilde{P}_m} = 1 - f. \tag{5}$$

Here, f is the fraction of the precipitation rate at the melting level P_m, which is carried from the convective region, P_s is the precipitation rate at the lowest observable level, and tildes denote the variables in the

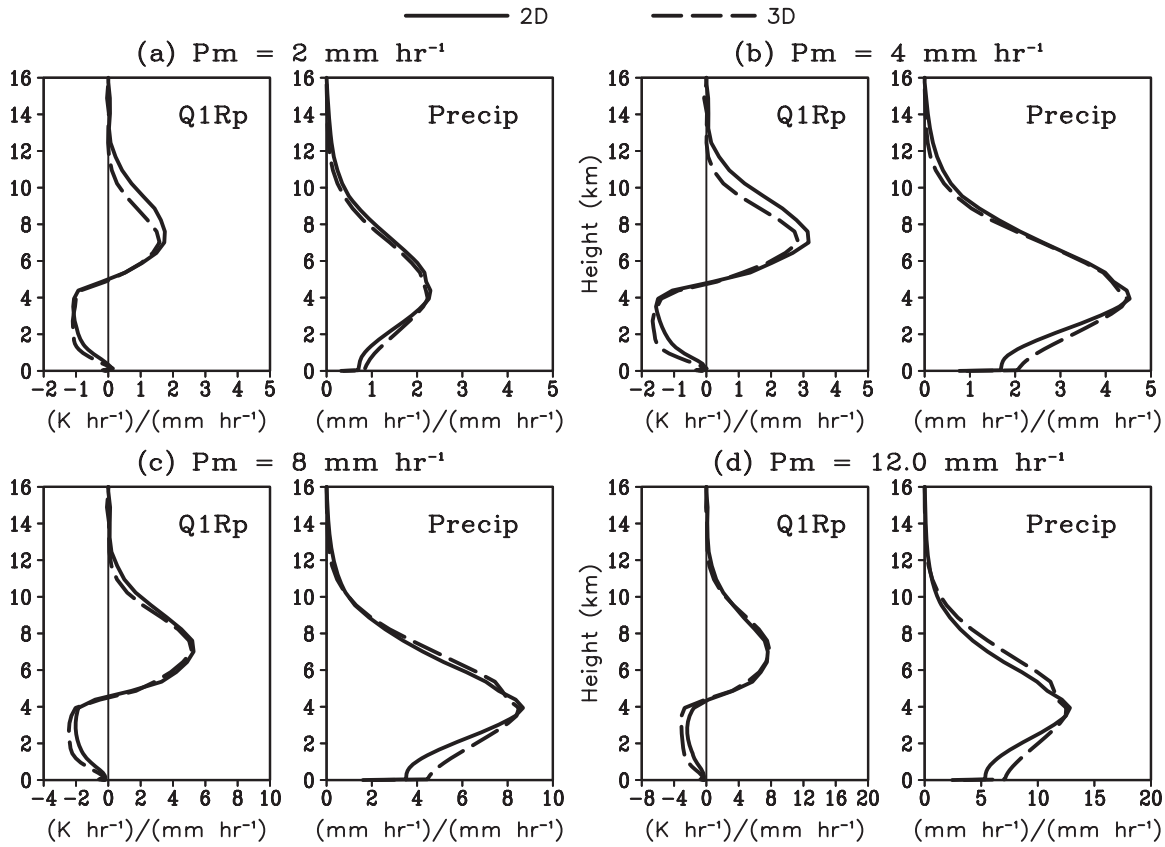

FIG. 10. Ensemble-mean GCE-simulated Q_{1Rp} and precipitation profiles with the selected P_m values of (a) 2.0 mm h^{-1}, (b) 4.0 mm h^{-1}, (c) 8.0 mm h^{-1}, and (d) 12 mm h^{-1} from the stratiform regions of 2D and 3D simulations.

lookup table. Figure 11 indicates that R_{conv} values are larger than unity and R_{stra} values are smaller than unity for both the LUT2D and LUT3D, which indicates the contribution to the anvil water budget made by the horizontal transfer of condensate from the convective region (i.e., $f > 0$). However, there are big differences in R_{conv} and R_{stra} between the LUT2D and LUT3D. The R_{conv} for the LUT2D decreases with the PTH, but R_{conv} for the LUT3D increases with the PTH higher than 5 km. Total condensates generated in deep convection are much larger than surface precipitation in the LUT3D, which results in large R_{conv}. On the other hand, R_{stra} values from the LUT3D are smaller than those from the LUT2D in the range 1 mm h^{-1} $< \tilde{P}_m \leq$ 8 mm h^{-1}. Thus more condensate is carried from the deep convective region to the stratiform region in the 3D model than is carried in the 2D model. It should be noted that R_{conv} and R_{stra} values do not strictly represent the horizontal transfer of condensate from the convective region to the stratiform region, because evaporation to the environment from the convective and stratiform regions is not taken into account. However, the evaporation to the environment from the convective and stratiform regions is much smaller than the horizontal transfer of condensate from the convective region to the stratiform region (Leary and Houze 1980; Chong and Hauser 1989; Tao et al. 1993b; Caniaux et al. 1994), and neglecting this term does not affect the above statement about the horizontal transfer of condensate from the convective region to the stratiform region. The energy budgets of the simulations are primarily a response to the imposed large-scale forcing. Therefore, if the upper-level heating associated with deep convection increases, the upper-level heating in the stratiform region naturally decreases, and the horizontal transfer of condensate from the convective region to the stratiform region increases.

Takayabu (2002) obtained a spectral expression of precipitation profiles to examine convective and stratiform rain characteristics as a function of the PTH over the equatorial area (10°N–10°S) observed by the TRMM PR. Precipitation profiles with a 0.3 mm h^{-1} precipitation-top threshold were accumulated and stratified according to PTHs. In her study, nadir data from PR2A25 version 5

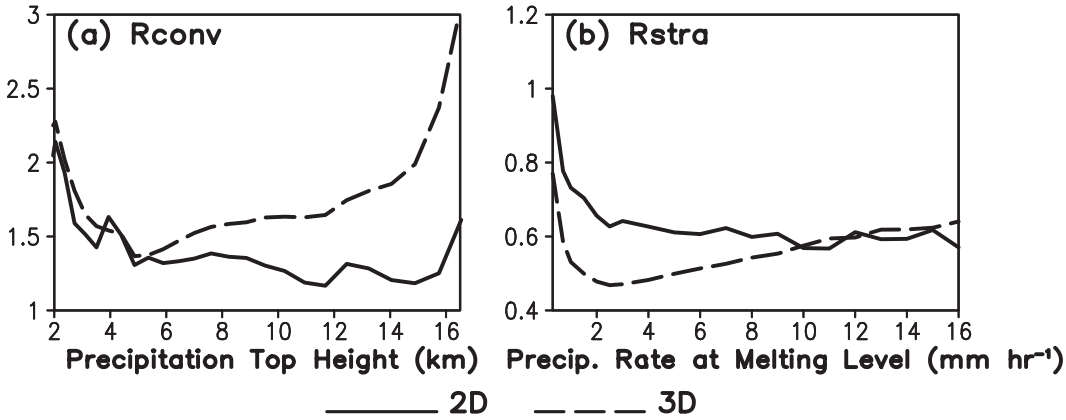

FIG. 11. The ratios R_{conv} and R_{stra} defined as Eqs. (4) and (5) for lookup tables from GCE 2D and 3D simulations (Figs. 2 and 3).

(Iguchi et al. 2000) for the period of 1998–99 were used, and convective and stratiform precipitations were separated based on the TRMM PR version 5 2A23 convective–stratiform separation algorithm. Following the suggestion of Schumacher and Houze (2003), the spectral plots of Takayabu (2002, Fig. 1) were revised by reclassifying shallow, isolated rain (rain type 15 in product 2A-23) as convective in Part I (Fig. 1 in Part I) and Yokoyama and Takayabu (2008, Fig. 5). Part I showed that spectral properties of GCE-simulated convective precipitation profiles correspond well to those of TRMM PR-observed profiles, having a smooth increase in precipitation intensity with increasing PTH. In this study, we obtained the spectral plots of convective precipitation profiles simulated in 2D and 3D models (Figs. 12b,c) to compare them against a spectral plot of TRMM PR-observed convective precipitation profiles (Fig. 12a). Here, nadir data from PR2A25 version 6 at "ocean" pixels over the western Pacific (5°N–15°S, 150°–180°E), which roughly corresponds to the TOGA COARE region, for December–February during 1998–2006 were used to obtain the spectral plot of TRMM PR-observed convective precipitation profiles. Forty percent of convective rain in the 2D model is shallow and congestus rain with PTH values lower than melting levels (about 4 km), which is consistent with TRMM PR observations. On the other hand, much (80%) of convective rain in the 3D model is deep convection with PTH values higher than the melting levels, and only 20% of convective rain is shallow and congestus rain with PTH values lower than the melting levels. This is consistent with the results from Phillips and Donner (2006), who found that the weak ascent ($0.1 < w < \sim 1$ m s^{-1}) outside the rapid convective updrafts is less prevalent in the 3D model than it is in the 2D model. For both 2D and 3D models, precipitation rates of the deep convection with PTH values higher than the melting levels are stronger than those of the PR-observed ones, which could be due to the model physics, especially ice parameterization.

In this study, a 2-km horizontal grid spacing is used for the 3D simulations because of the great computational demands of the 3D integrations. As already noted, test 3D simulations with a 1-km horizontal grid spacing indicated that basic features do not change with such a change in resolution. However, the GCE model results reported in Grabowski et al. (2006) showed that using a finer resolution (250 m versus 1000 m) resulted in a smoother transition to deep convection in diurnal convective growth during the TRMM LBA experiment in Brazil. Lang et al. (2007) showed that the convective intensity in the 250-m simulation is steadier than the more pulse-like intensity in the 1000-m run for convective systems during the TRMM LBA. They suggested the horizontal resolutions normally used to simulate deep convection (i.e., 1 km or coarser) are inadequate for the diurnal growth of convection in this type of environment and that finer resolutions are needed. Comparisons of the LUT2D and LUT3D in this study suggest that a horizontal resolution of 1 km or coarser is also inadequate for oceanic convective systems. Coarser-resolution simulation produces wider clouds, and this has a direct impact on cloud entrainment, leading to fewer, more-concentrated convective cores that ascend higher into the troposphere. Thus the 3D model with coarser resolution is inherently limited in its ability to produce shallow convection and congestus-type clouds. More-concentrated convective cores produce more ice-phase condensates, which are generated in and carried from the convective region to the stratiform region, and less condensate is produced by the stratiform region's own upward motion (Fig. 13).

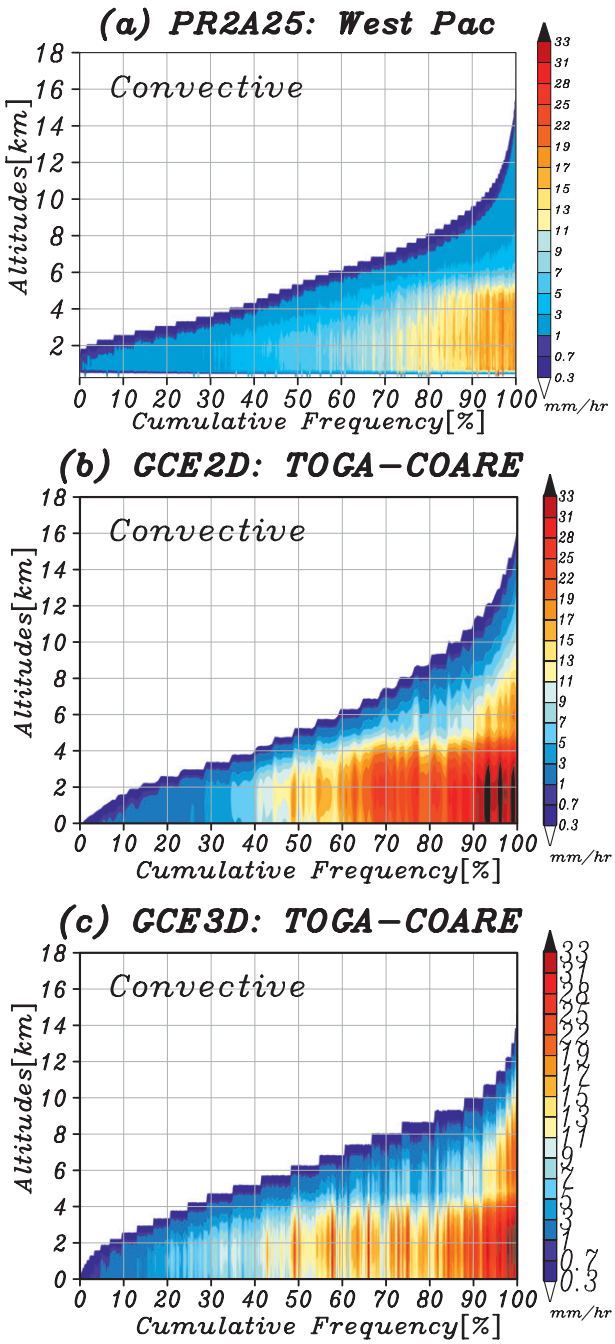

FIG. 12. Spectral plots of convective precipitation profiles stratified by PTH for (a) TRMM PR-observed precipitation profiles, using nadir data from PR2A25 version 6 at "ocean" pixels over the western Pacific (5°N–15°S, 150°–180°E), which roughly corresponds to the TOGA COARE region, for December–February during 1998–2006; (b) the GCE 2D model-simulated profiles; (c) the GCE 3D model-simulated profiles. The abscissa is cumulative frequency and the ordinate is altitude; the precipitation rate is indicated with color. A threshold of 0.3 mm h^{-1} is used for the precipitation-top detection.

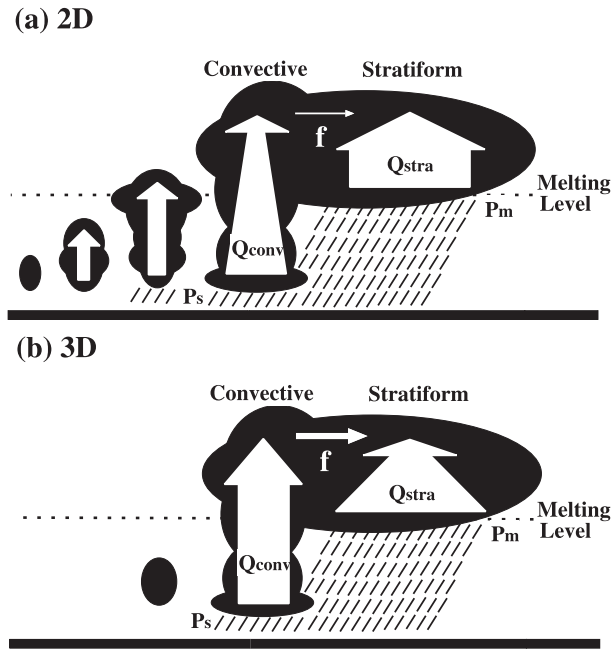

FIG. 13. Schematic view of the water budget of a mesoscale convective system in (a) 2D and (b) 3D simulations.

5. Summary and future work

The SLH algorithm has been developed for the TRMM PR using a 2D version of the GCE model. Real clouds and cloud systems are 3D. The availability of exponentially increasing computer capabilities has resulted in 3D CRM simulations for multiday periods with large horizontal domains becoming increasing prevalent. In this paper, the SLH algorithm is applied to PR data using LUTs derived from 2D simulations (LUT2D) and GCE 3D simulations (LUT3D) from TOGA COARE, and the results are compared with heating profiles derived diagnostically from sounding data from SCSMEX.

Using the LUT3D leads to less agreement between the SLH-retrieved Q_{1Rp} and sounding-based Q_1. The level of maximum heating of $Q_{1Rp} + Q_R$ is slightly lower than that of the sounding-derived Q_1. This is explained by the fact that using the LUT3D gives stronger convective heating and weaker stratiform heating above the melting level than using the LUT2D does. Condensate carried from the deep convective region to the stratiform region is larger in the 3D model than in the 2D model, and there is less condensate produced by the stratiform region's own upward motion in the 3D model. The argument that the 2D LUT retrieval generally compares better to the sounding-derived Q_1 from SCSMEX than the LUT 3D retrieval is consistent with the previous ground-based observations and recent

TRMM observations, which suggest that the primary precipitation mechanism in deep oceanic convection is the liquid water processes.

In this study, the horizontal grid spacing is chosen as 2 km for the 3D simulations because of the great computational demands of the 3D integrations. Coarser-resolution simulation produces wider clouds, and this has a direct impact on cloud entrainment, leading to fewer, more-concentrated convective cores that ascend higher into the troposphere. More-concentrated convective cores produce more ice-phase condensates, which are generated in and carried from the convective region to the stratiform region, and there is less condensate produced by the stratiform region's own upward motion. The 3D simulation with finer resolution (i.e., 250-m resolution) is computationally expensive because finer resolution requires smaller time steps. The model domain was 64 km $\times$ 64 km for the 250-m simulation of Lang et al. (2007). Such small domain size is adequate for the weakly organized convection examined in Lang et al. (2007) but inadequate for the organized convection examined here. In the future, we will conduct the 3D simulations with finer resolution and large domain size using a supercomputer. There are also plans to compare the SLH estimates from ground radar data, with heating profiles derived from sounding data and other observations using the variational analysis approach of Zhang and Lin (1997), to avoid the sampling errors.

Acknowledgments. This study is supported by the JAXA/EORC Tropical Rainfall Measuring Mission (TRMM) project. The authors thank Prof. C. Schumacher and an anonymous reviewer for their constructive comments that improved the clarity of the presentation in this paper.

REFERENCES

Awaka, J., H. Kumagai, T. Iguchi, and K. Okamoto, 1996: Development of an algorithm for classifying rain types (in Japanese). *J. Commun. Res. Lab.,* **42,** 325–337.

——, T. Iguchi, and K. Okamoto, 1998: Early results on rain type classification by the Tropical Rainfall Measuring Mission (TRMM) precipitation radar. *Proc. Eighth URSI Commission F Open Symp.,* Aveiro, Portugal, URSI, 143–146.

——, ——, and ——, 2007: Rain type classification algorithm. *Measuring Precipitation from Space—EURAINSAT and the Future,* V. Levizzani, P. Bauer, and F. J. Turk, Eds., Springer, 213–224.

——, ——, and ——, 2009: TRMM PR standard algorithm 2A23 and its performance on bright band detection. *J. Meteor. Soc. Japan,* **87,** 31–52.

Bauer, P., 2001: Over-ocean rainfall retrieval from multisensor data of the tropical rainfall measuring mission. Part I: Design and evaluation of inversion databases. *J. Atmos. Oceanic Technol.,* **18,** 1315–1330.

Biggerstaff, M. I., E.-K. Seo, S. Hristova-Veleva, and K.-Y. Kim, 2006: Impact of cloud model microphysics on passive microwave retrievals of cloud properties. Part I: Model comparison using EOF analyses. *J. Appl. Meteor. Climatol.,* **45,** 930–954.

Caniaux, G., J.-L. Redelsperger, and J.-P. Lafore, 1994: A numerical study of the stratiform region of a fast-moving squall line. Part I: General description and water and heat budgets. *J. Atmos. Sci.,* **51,** 2046–2074.

Chong, M., and D. Hauser, 1989: A tropical squall line observed during the COPT81 experiment in West Africa. Part II: Water budget. *Mon. Wea. Rev.,* **117,** 728–744.

Ciesielski, P. E., and R. H. Johnson, 2006: Contrasting characteristics of convection over the northern and southern South China Sea during SCSMEX. *Mon. Wea. Rev.,* **134,** 1041–1062.

——, ——, P. T. Haertel, and J. Wang, 2003: Corrected TOGA COARE sounding humidity data: Impact on diagnosed properties of convection and climate over the warm pool. *J. Climate,* **16,** 2370–2384.

DeMott, C. A., and S. A. Rutledge, 1998: The vertical structure of TOGA COARE convection. Part I: Radar echo distribution. *J. Atmos. Sci.,* **55,** 2730–2747.

Donner, L. J., C. J. Seman, and R. S. Hemler, 1999: Three-dimensional cloud-system modeling of GATE convection. *J. Atmos. Sci.,* **56,** 1885–1912.

Emanuel, K. A., and M. Zivkovic-Rothman, 1999: Development and evaluation of a convection scheme for use in climate models. *J. Atmos. Sci.,* **56,** 1766–1782.

Fairall, C., E. F. Bradley, D. P. Rogers, J. B. Edson, and G. S. Young, 1996: Bulk parameterization of air–sea fluxes for TOGA COARE. *J. Geophys. Res.,* **101,** 3747–3764.

Gamache, J. F., and R. A. Houze Jr., 1983: Water budget of a mesoscale convective system in the tropics. *J. Atmos. Sci.,* **40,** 1835–1850.

Grabowski, W. W., 2001: Coupling cloud processes with the large-scale dynamics using the Cloud-Resolving Convection Parameterization (CRCP). *J. Atmos. Sci.,* **58,** 978–997.

——, and P. K. Smolarkiewicz, 1999: CRCP: A cloud resolving convection parameterization for modeling the tropical convective atmosphere. *Physica D,* **133,** 171–178.

——, X. Wu, and M. W. Moncrieff, 1996: Cloud-resolving modeling of tropical cloud systems during Phase III of GATE. Part I: Two-dimensional experiments. *J. Atmos. Sci.,* **53,** 3684–3709.

——, ——, ——, and W. D. Hall, 1998: Cloud-resolving modeling of tropical cloud systems during Phase III of GATE. Part II: Effects of resolution and the third spatial dimension. *J. Atmos. Sci.,* **55,** 3264–3282.

——, and Coauthors, 2006: Daytime convective development over land: A model intercomparison based on LBA observations. *Quart. J. Roy. Meteor. Soc.,* **132,** 317–344.

Grecu, M., and W. S. Olson, 2006: Bayesian estimation of precipitation from satellite passive microwave observations using combined radar–radiometer retrievals. *J. Appl. Meteor. Climatol.,* **45,** 416–433.

Hartmann, D., H. H. Hendon, and R. A. Houze Jr., 1984: Some implications of the mesoscale circulations in tropical cloud clusters for large-scale dynamics and climate. *J. Atmos. Sci.,* **41,** 113–121.

Haynes, P. H., and M. E. McIntyre, 1987: On the evolution of vorticity and potential vorticity in the presence of diabatic heating and frictional or other forces. *J. Atmos. Sci.,* **44,** 828–841.

Heymsfield, G. M., B. Geerts, and L. Tian, 2000: TRMM precipitation radar reflectivity profiles as compared with high-resolution

airborne and ground-based radar measurements. *J. Appl. Meteor.,* **39,** 2080–2102.

Holloway, C. E., and J. D. Neelin, 2007: The convective cold top and quasi equilibrium. *J. Atmos. Sci.,* **64,** 1467–1487.

Houze, R. A., Jr., 1982: Cloud clusters and large-scale vertical motions in the tropics. *J. Meteor. Soc. Japan,* **60,** 396–410.

——, 1989: Observed structure of mesoscale convective systems and implications for large-scale heating. *Quart. J. Roy. Meteor. Soc.,* **115,** 425–461.

——, 1997: Stratiform precipitation in regions of convection: A meteorological paradox. *Bull. Amer. Meteor. Soc.,* **78,** 2179–2196.

——, 2004: Mesoscale convective systems. *Rev. Geophys.,* **42,** RG4003, doi:10.1029/2004RG000150.

——, C.-P. Cheng, C. A. Leary, and J. F. Gamache, 1980: Diagnosis of cloud mass and heat fluxes from radar and synoptic data. *J. Atmos. Sci.,* **37,** 754–773.

Iguchi, T., 2007: Space-borne radar algorithms. *Measuring Precipitation from Space—EURAINSAT and the Future,* V. Levizzani, P. Bauer, and F. J. Turk, Eds., Springer, 199–212.

——, T. Kozu, R. Meneghini, J. Awaka, and K. Okamoto, 2000: Rain-profiling algorithm for the TRMM precipitation radar. *J. Appl. Meteor.,* **39,** 2038–2052.

——, ——, J. Kwiatkowski, R. Meneghini, J. Awaka, and K. Okamoto, 2009: Uncertainties in the rain profiling algorithm for the TRMM precipitation radar. *J. Meteor. Soc. Japan,* **87,** 1–30.

Johnson, R. H., 1984: Partitioning tropical heat and moisture budgets into cumulus and mesoscale components: Implications for cumulus parameterization. *Mon. Wea. Rev.,* **112,** 1590–1601.

——, 2006: Mesoscale processes. *The Asian Monsoon,* B. Wang, Ed., Praxis, 331–356.

——, and D. C. Kriete, 1982: Thermodynamic and circulation characteristics of winter monsoon tropical mesoscale convection. *Mon. Wea. Rev.,* **110,** 1898–1911.

——, and G. S. Young, 1983: Heat and moisture budgets of tropical mesoscale anvil clouds. *J. Atmos. Sci.,* **40,** 2138–2146.

——, and X. Lin, 1997: Episodic trade wind regimes over the western Pacific warm pool. *J. Atmos. Sci.,* **54,** 2020–2034.

——, and P. E. Ciesielski, 2002: Characteristics of the 1998 summer monsoon onset over the northern South China Sea. *J. Meteor. Soc. Japan,* **80,** 561–578.

Jorgensen, D. P., and M. A. LeMone, 1989: Vertically velocity characteristics of oceanic convection. *J. Atmos. Sci.,* **46,** 621–640.

Kozu, T., and Coauthors, 2001: Development of precipitation radar onboard the Tropical Rainfall Measuring Mission (TRMM) satellite. *IEEE Trans. Geosci. Remote Sens.,* **39,** 102–116.

Kummerow, C., and Coauthors, 2000: The status of the Tropical Rainfall Measuring Mission (TRMM) after two years in orbit. *J. Appl. Meteor.,* **39,** 1965–1982.

Lang, S., W.-K. Tao, J. Simpson, and B. Ferrier, 2003: Modeling of convective–stratiform precipitation processes: Sensitivity to partitioning methods. *J. Appl. Meteor.,* **42,** 505–527.

——, ——, R. Cifelli, W. Olson, J. Halverson, S. Rutledge, and J. Simpson, 2007: Improving simulations of convective systems from TRMM LBA: Easterly and westerly regimes. *J. Atmos. Sci.,* **64,** 1141–1164.

Lau, K., and Coauthors, 2000: A report of the field operations and early results of the South China Sea Monsoon Experiment (SCSMEX). *Bull. Amer. Meteor. Soc.,* **81,** 1261–1270.

Leary, C. A., and R. A. Houze Jr., 1979: Melting and evaporation of hydrometeors in precipitation from the anvil clouds of deep tropical convection. *J. Atmos. Sci.,* **36,** 669–679.

——, and ——, 1980: The contribution of mesoscale motions to the mass and heat fluxes of an intense tropical convective system. *J. Atmos. Sci.,* **37,** 784–796.

L'Ecuyer, T. S., and G. L. Stephens, 2003: The tropical ocean energy budget from the TRMM perspective. Part I: Algorithm and uncertainties. *J. Climate,* **16,** 1967–1985.

Lin, X., and R. H. Johnson, 1996: Kinematic and thermodynamic characteristics of the flow over the western Pacific warm pool during TOGA COARE. *J. Atmos. Sci.,* **53,** 695–715.

Lin, Y.-L., R. D. Farley, and H. D. Orville, 1983: Bulk parameterization of the snow field in a cloud model. *J. Climate Appl. Meteor.,* **22,** 1065–1092.

Magagi, R., and A. P. Barros, 2004: Estimation of latent heating of rainfall during the onset of the Indian monsoon using TRMM PR and radiosonde data. *J. Appl. Meteor.,* **43,** 328–349.

Mapes, B. E., 2001: Water's two height scales: The moist adiabat and the radiative troposphere. *Quart. J. Roy. Meteor. Soc.,* **127,** 2253–2266.

——, P. E. Ciesielski, and R. H. Johnson, 2003: Sampling errors in rawinsonde-array budgets. *J. Atmos. Sci.,* **60,** 2697–2714.

Nakajima, K., and T. Matsuno, 1988: Numerical experiments concerning the origin of cloud clusters in the tropics. *J. Meteor. Soc. Japan,* **66,** 309–329.

Negri, A. J., T. L. Bell, and L. Xu, 2002: Sampling of the diurnal cycle of precipitation using TRMM. *J. Atmos. Oceanic Technol.,* **19,** 1333–1344.

Nesbitt, S. W., E. J. Zipser, and D. J. Cecil, 2000: A census of precipitation features in the tropics using TRMM: Radar, ice scattering, and lightning observations. *J. Climate,* **13,** 4087–4106.

Nitta, T., and S. Esbensen, 1974: Heat and moisture budget analyses using BOMEX data. *Mon. Wea. Rev.,* **102,** 17–28.

Okamoto, K., 2003: A short history of the TRMM precipitation radar. *Cloud Systems, Hurricanes and the Tropical Rainfall Measurement Mission (TRMM): A Tribute to Dr. Joanne Simpson, Meteor. Monogr.,* No. 51, Amer. Meteor. Soc., 187–195.

——, and S. Shige, 2008: TRMM precipitation radar and its observation results (in Japanese). *IEICE Trans. Commun.,* **J91-B,** 723–733.

Pandya, R. E., and D. R. Durran, 1996: The influence of convectively generated thermal forcing on the mesoscale circulation around squall lines. *J. Atmos. Sci.,* **53,** 2924–2951.

Petersen, W. A., and S. A. Rutledge, 2001: Regional variability in tropical convection: Observations from TRMM. *J. Climate,* **14,** 3566–3586.

Phillips, V. T. J., and L. J. Donner, 2006: Cloud microphysics, radiation and vertical velocities in two- and three-dimensional simulations of deep convection. *Quart. J. Roy. Meteor. Soc.,* **132,** 3011–3033.

Pielke, R. A., Sr., and Coauthors, 2006: A new paradigm for parameterizations in numerical weather prediction and other atmospheric models. *Natl. Wea. Dig.,* **30,** 93–99.

——, and Coauthors, 2007: Satellite-based model parameterization of diabatic heating. *Eos, Trans. Amer. Geophys. Union,* **88,** 96–97, doi:10.1029/2007EO080003.

Randall, D., M. Khairoutdinov, A. Arakawa, and W. Grabowski, 2003: Breaking the cloud parameterization deadlock. *Bull. Amer. Meteor. Soc.,* **84,** 1547–1564.

Rutledge, S. A., and P. V. Hobbs, 1984: The mesoscale and microscale structure and organization of clouds and precipitation in midlatitude cyclones. XII: A diagnostic modeling study of precipitation development in narrow cold-frontal rainbands. *J. Atmos. Sci.,* **41,** 2949–2972.

Schlesinger, R. E., 1984: Effects of the pressure perturbation field in numerical models of unidirectionally sheared thunderstorm convection: Two versus three dimensions. *J. Atmos. Sci.,* **41,** 1571–1587.

Schumacher, C., and R. A. Houze Jr., 2000: Comparison of radar data from the TRMM satellite and Kwajalein oceanic validation site. *J. Appl. Meteor.,* **39,** 2151–2164.

——, and ——, 2003: The TRMM precipitation radar's view of shallow, isolated rain. *J. Appl. Meteor.,* **42,** 1519–1524.

——, ——, and I. Kraucunas, 2004: The tropical dynamical response to latent heating estimates derived from the TRMM precipitation radar. *J. Atmos. Sci.,* **61,** 1341–1358.

——, M. H. Zhang, and P. E. Ciesielski, 2007: Heating structures of the TRMM field campaigns. *J. Atmos. Sci.,* **64,** 2593–2610.

——, ——, and ——, 2008: Tropical cloud heating profiles: Analysis from KWAJEX. *Mon. Wea. Rev.,* **136,** 4289–4300.

Seo, E.-K., and M. I. Biggerstaff, 2006: Impact of cloud model microphysics on passive microwave retrievals of cloud properties. Part II: Uncertainty in rain, hydrometeor structure, and latent heating retrievals. *J. Appl. Meteor. Climatol.,* **45,** 955–972.

Shige, S., and T. Satomura, 2000: The gravity wave response in the troposphere around deep convection. *J. Meteor. Soc. Japan,* **78,** 789–801.

——, Y. N. Takayabu, W.-K. Tao, and D. E. Johnson, 2004: Spectral retrieval of latent heating profiles from TRMM PR data. Part I: Development of a model-based algorithm. *J. Appl. Meteor.,* **43,** 1095–1113.

——, ——, ——, and C.-L. Shie, 2007: Spectral retrieval of latent heating profiles from TRMM PR data. Part II: Algorithm improvement and heating estimates over tropical ocean regions. *J. Appl. Meteor. Climatol.,* **46,** 1098–1124.

——, ——, and ——, 2008: Spectral retrieval of latent heating profiles from TRMM PR data. Part III: Estimating apparent moisture sink profiles over tropical oceans. *J. Appl. Meteor. Climatol.,* **47,** 620–640.

Simpson, J., R. F. Adler, and G. R. North, 1988: A proposed satellite Tropical Rainfall Measuring Mission (TRMM). *Bull. Amer. Meteor. Soc.,* **69,** 278–295.

——, C. Kummerow, W.-K. Tao, and R. F. Adler, 1996: On the Tropical Rainfall Measuring Mission (TRMM). *Meteor. Atmos. Phys.,* **60,** 19–36.

Soong, S.-T., and Y. Ogura, 1980: Response of tradewind cumuli to large-scale processes. *J. Atmos. Sci.,* **37,** 2035–2050.

——, and W.-K. Tao, 1980: Response of deep tropical cumulus clouds to mesoscale processes. *J. Atmos. Sci.,* **37,** 2016–2034.

Sui, C.-H., K.-M. Lau, W.-K. Tao, and J. Simpson, 1994: The tropical water and energy cycles in a cumulus ensemble model. Part I: Equilibrium climate. *J. Atmos. Sci.,* **51,** 711–728.

Szoke, E. J., E. J. Zipser, and D. P. Jorgensen, 1986: A radar study of convective cells in mesoscale systems in GATE. Part I: Vertical profile statistics and comparison with hurricanes. *J. Atmos. Sci.,* **43,** 182–198.

Takahashi, T., K. Suzuki, M. Orita, M. Tokuno, and R. de la Mar, 1995: Videosonde observations of precipitation processes in equatorial cloud clusters. *J. Meteor. Soc. Japan,* **73,** 509–534.

Takayabu, Y. N., 2002: Spectral representation of rain features and diurnal variations observed with TRMM PR over the equatorial area. *Geophys. Res. Lett.,* **29,** 1584, doi:10.1029/2001GL014113.

——, 2006: Rain-yield per flash calculated from TRMM PR and LIS data and its relationship to the contribution of tall convective rain. *Geophys. Res. Lett.,* **33,** L18705, doi:10.1029/2006GL027531.

Tao, W.-K., 2007: Cloud resolving modeling. *J. Meteor. Soc. Japan,* **85,** 305–330.

——, and S.-T. Soong, 1986: A study of the response of deep tropical clouds to mesoscale processes: Three-dimensional numerical experiments. *J. Atmos. Sci.,* **43,** 2653–2676.

——, and J. Simpson, 1993: Goddard Cumulus Ensemble model. Part I: Model description. *Terr. Atmos. Ocean. Sci.,* **4,** 35–72.

——, S. Lang, J. Simpson, and R. Adler, 1993a: Retrieval algorithms for estimating the vertical profiles of latent heat release: Their applications for TRMM. *J. Meteor. Soc. Japan,* **71,** 685–700.

——, J. Simpson, C.-H. Sui, B. Ferrier, S. Lang, J. Scala, M.-D. Chou, and K. Pickering, 1993b: Heating, moisture, and water budgets of tropical and midlatitude squall lines: Comparisons and sensitivity to long radiation. *J. Atmos. Sci.,* **50,** 673–690.

——, S. Lang, J. Simpson, W. Olson, D. Johnson, B. Ferrier, C. Kummerow, and R. Adler, 2000: Vertical profiles of latent heat release and their retrieval for TOGA COARE convective systems using a cloud resolving model, SSM/I, and shipborne radar data. *J. Meteor. Soc. Japan,* **78,** 333–355.

——, and Coauthors, 2003a: Microphysics, radiation and surface processes in the Goddard Cumulus Ensemble (GCE) model. *Meteor. Atmos. Phys.,* **82,** 97–137.

——, C.-L. Shie, J. Simpson, S. Braun, R. H. Johnson, and P. E. Ciesielski, 2003b: Convective systems over the South China Sea: Cloud-resolving model simulations. *J. Atmos. Sci.,* **60,** 2929–2956.

——, D. Johnson, C.-L. Shie, and J. Simpson, 2004: The atmospheric energy budget and large-scale precipitation efficiency of convective systems during TOGA COARE, GATE, SCSMEX, and ARM: Cloud-resolving model simulations. *J. Atmos. Sci.,* **61,** 2405–2423.

——, and Coauthors, 2006: Retrieval of latent heating from TRMM measurements. *Bull. Amer. Meteor. Soc.,* **87,** 1555–1572.

Wang, J., H. L. Cole, D. J. Carlson, E. R. Miller, K. Beierle, A. Paukkunen, and T. K. Laine, 2002: Corrections of humidity measurement errors from Vaisala RS80 radiosonde—Application to TOGA COARE data. *J. Atmos. Oceanic Technol.,* **19,** 981–1002.

Wang, Y., W.-K. Tao, and J. Simpson, 1996: The impact of ocean surface fluxes on a TOGA COARE cloud system. *Mon. Wea. Rev.,* **124,** 2753–2763.

Webster, P. J., and R. Lukas, 1992: TOGA COARE: The coupled ocean–atmosphere response experiment. *Bull. Amer. Meteor. Soc.,* **73,** 1377–1416.

Wiedner, M., C. Prigent, J. R. Pardo, O. Nuissier, J.-P. Chaboureau, J.-P. Pinty, and P. Mascart, 2004: Modeling of passive microwave responses in convective situations using output from mesoscale models: Comparison with TRMM/TMI satellite observations. *J. Geophys. Res.,* **109,** D06214, doi:10.1029/2003JD004280.

Wilhelmson, R., 1974: The life cycle of a thunderstorm in three dimensions. *J. Atmos. Sci.,* **31,** 1629–1651.

Wu, X., M. W. Moncrieff, and K. A. Emanuel, 2000: Evaluation of large-scale forcing during TOGA COARE for cloud-resolving models and single-column models. *J. Atmos. Sci.,* **57,** 2977–2985.

Xu, K.-M., 1993: Cumulus ensemble simulation. *The Representation of Cumulus Convection in Numerical Models, Meteor. Monogr.,* No. 46, Amer. Meteor. Soc., 221–235.

Yamasaki, M., 1975: A numerical experiment of the interaction between cumulus convection and large-scale motion. *Pap. Meteor. Geophys.,* **26,** 63–91.

Yanai, M., and R. H. Johnson, 1993: Impacts of cumulus convection on thermodynamic fields. *The Representation of Cumulus*

Convection in Numerical Models, Meteor. Monogr., No. 46, Amer. Meteor. Soc., 39–62.

——, S. Esbensen, and J.-H. Chu, 1973: Determination of bulk properties of tropical cloud clusters from large-scale heat and moisture budgets. *J. Atmos. Sci.,* **30,** 611–627.

Yang, S., W. Olson, J. J. Wang, T. L. Bell, E. A. Smith, and C. D. Kummerow, 2006: Precipitation and latent heating distributions from satellite passive microwave radiometry. Part II: Evaluation of estimates using independent data. *J. Appl. Meteor. Climatol.,* **45,** 721–739.

Yokoyama, C., and Y. N. Takayabu, 2008: A statistical study on rain characteristics of tropical cyclones using TRMM satellite data. *Mon. Wea. Rev.,* **136,** 3848–3862.

Zeng, X., and Coauthors, 2007: Evaluating clouds in long-term cloud-resolving model simulations with observational data. *J. Atmos. Sci.,* **64,** 4153–4177.

——, W.-K. Tao, S. Lang, A. Y. Hou, M. Zhang, and J. Simpson, 2008: On the sensitivity of atmospheric ensembles to cloud microphysics in long-term cloud-resolving model. *J. Meteor. Soc. Japan,* **86,** 45–65.

Zhang, M. H., and J. L. Lin, 1997: Constrained variational analysis of sounding data based on column-integrated budgets of mass, heat, moisture, and momentum: Approach and application to arm measurements. *J. Atmos. Sci.,* **54,** 1503–1524.

Zhou, Y. P., and Coauthors, 2007: Use of high-resolution satellite observations to evaluate cloud and precipitation statistics from cloud-resolving model simulations. Part I: South China Sea Monsoon Experiment. *J. Atmos. Sci.,* **64,** 4309–4329.

Zipser, E. J., and K. R. Lutz, 1994: The vertical profile of radar reflectivity of convective cells: A strong indicator of storm intensity and lightning probability? *Mon. Wea. Rev.,* **122,** 1751–1759.